

Fully digital, urban networked staring radar

Griffiths, Darren; Jahangir, Mohammed; Kannanthara, Jithin; Donlan, Gwynfor; Baker, Chris J.; Antoniou, Michail; Singh, Yeshpal

DOI:

[10.1049/rsn2.12499](https://doi.org/10.1049/rsn2.12499)

License:

Creative Commons: Attribution (CC BY)

Document Version

Publisher's PDF, also known as Version of record

Citation for published version (Harvard):

Griffiths, D, Jahangir, M, Kannanthara, J, Donlan, G, Baker, CJ, Antoniou, M & Singh, Y 2023, 'Fully digital, urban networked staring radar: Simulation and experimentation', *IET Radar, Sonar & Navigation*, pp. 1-17. <https://doi.org/10.1049/rsn2.12499>

[Link to publication on Research at Birmingham portal](#)

General rights

Unless a licence is specified above, all rights (including copyright and moral rights) in this document are retained by the authors and/or the copyright holders. The express permission of the copyright holder must be obtained for any use of this material other than for purposes permitted by law.

- Users may freely distribute the URL that is used to identify this publication.
- Users may download and/or print one copy of the publication from the University of Birmingham research portal for the purpose of private study or non-commercial research.
- User may use extracts from the document in line with the concept of 'fair dealing' under the Copyright, Designs and Patents Act 1988 (?)
- Users may not further distribute the material nor use it for the purposes of commercial gain.

Where a licence is displayed above, please note the terms and conditions of the licence govern your use of this document.

When citing, please reference the published version.

Take down policy

While the University of Birmingham exercises care and attention in making items available there are rare occasions when an item has been uploaded in error or has been deemed to be commercially or otherwise sensitive.

If you believe that this is the case for this document, please contact UBIRA@lists.bham.ac.uk providing details and we will remove access to the work immediately and investigate.

ORIGINAL RESEARCH

Fully digital, urban networked staring radar: Simulation and experimentation

Darren Griffiths¹  | Mohammed Jahangir²  | Jithin Kannanthara¹  |
Gwynfor Donlan¹ | Chris J. Baker² | Michail Antoniou² | Yeshpal Singh¹

¹School of Physics and Astronomy, University of Birmingham, Birmingham, UK

²School of Electronic, Electrical and Systems Engineering, University of Birmingham, Birmingham, UK

Correspondence

Darren Griffiths.
Email: dsg066@student.bham.ac.uk

Funding information

Defence Science and Technology Laboratory; UK National Quantum Technology Hub in Sensing and Timing, Grant/Award Number: EP/T001046/1

Abstract

The application and uses of drones in all areas are continuously rising, especially in civilian use cases. This increasing threat requires reliable drone surveillance in urban environments. Radar is the obvious candidate with its ability to detect small objects at range, in all weather conditions. The use of an L-band networked radar for urban sensing of S-UAS targets is explored. Small echoes from S-UAS places a premium on synchronisation, which is the fundamental key for high performance networked radar. The effect of timing errors on the operation of the network radar is investigated theoretically and experimentally, and the processing tools for synchronising data based on the direct signal returns of the transmitter are developed. Also, drone detection using bistatic L-band staring radar is achieved both in simulation and then in real field trials where the SNR and detection performance are computed and analysed. The updated direct signal synchronisation method for bistatic staring radar is shown to provide comparable SNR and positional accuracy for S-UAS targets as the monostatic staring radar.

KEYWORDS

distributed sensors, Doppler radar, micro Doppler, multistatic radar, oscillators, passive radar, performance evaluation, phase locked loops, phased array radar, synchronisation

1 | INTRODUCTION

In recent decades, sensors have improved in terms of their sensitivity to detecting small unmanned aircraft systems (S-UAS). This is matched by the increasing demand and usage of these systems. Drones are progressively being used in the rapid delivery of packages and recreational uses such as for photography and videography. However, drones themselves provide a huge security risk as they have the potential to be used for criminal activities and are difficult to detect [1, 2]. It is expected that the use of drones will increase by an order of magnitude over coming years, so more robust surveillance methods are required [3]. Radar is an emerging technology for the use of detection, tracking and classification of S-UAS [4–6] and has the capability to operate during night and in all weather conditions [7, 8]. One particular class of modern radars, active electronically scanned arrays (AESA) utilise a grid of

transceiver antennas with adjustable phase shifters [9] to swiftly change the pointing direction of the beam and this allows for more sophisticated signal processing techniques to improve the radar's effectiveness [10]. Drones occupy the same airspace as birds and share many of the same features when viewed by a radar (such as size, altitude and velocity) [11, 12] and therefore better classification capability is required to distinguish between bird and drone. Although the improved speed of AESAs allows for longer integration times, this can be further improved with staring radars which provide continuous illumination of the field of view (FOV) via a broad transmit beam, digitisation of the data from multiple beams simultaneously to enable digital beam forming on receive [13, 14]. The combined effect of the broad transmit beam and digital beamforming enables continuous dwell on multiple targets and further increases sensitivity of radar systems and allows for fine Doppler resolution. Digital array radars allow for greater flexibility, one

This is an open access article under the terms of the [Creative Commons Attribution](https://creativecommons.org/licenses/by/4.0/) License, which permits use, distribution and reproduction in any medium, provided the original work is properly cited.

© 2023 The Authors. *IET Radar, Sonar & Navigation* published by John Wiley & Sons Ltd on behalf of The Institution of Engineering and Technology.

example is shown in ref. [15] which is a 4×1 element linear receiver array at S-band and utilises digital beamforming on the recorded data to point the beam simultaneously in various directions. The system demonstrated detection of S-UAS targets up to 1.7 km. Another is the X-Band staring system (RAD-DAR) [16]. This system operates with frequency modulated continuous wave (FMCW) waveforms, contains a 64 element (8×8) digital receive antenna array and performs detection of drones up to 3 km with high location accuracy.

The L-band system used in the work presented in this paper, transmits a pulse waveform utilising a 64 element (4×16) digital receiver array, which is capable of drone detection up to a range of 5 km [11, 14, 17, 18].

The complexities such as slow velocities, multipath and impaired visibility at low altitudes due to other structures each offer additional challenge for the detection of S-UAVs. [19]. The use of radar networks are more resilient to these effects since they can extract target features from different viewpoints [20]. Other benefits of networked radar are that they can provide improved coverage by efficient positioning of sensor nodes [21], increased positional accuracy via combining multiple measurements and improved sensitivity due to more efficient collection of echoes [20]. These benefits can be achieved through the use of advanced signal processing and data fusion techniques [22].

While synchronisation is important for all radars between the transmitter and receiver subsystems, a physical timing link such as RF cabling may be impractical or prohibitively costly. Therefore, one of the main challenges of networked radar is to ensure a highly accurate (to at least a local time scale) or a common timing reference is available to each node. An additional consequence of a lack of inherent coherence between transmitter and receiver nodes is that there is no longer an effect of phase noise cancelation [23, 24]. A summary of time and frequency synchronisation requirements for bistatic radar is given in ref. [25]. A review of synchronisation protocols is presented in ref. [26] synchronisation where the different radars can be approximated as a wireless sensor network. But the methods in ref. [26] are limited to microsecond level synchronisation accuracy. Synchronisation errors and their impact in another pulsed radar system were analysed in ref. [27]. The impact of the loss of synchronisation of the signal to noise ratio (SNR) is calculated in ref. [28] in terms of the fraction of pulse overlap at the time of target reflection. Previous work, looking into the effect of synchronisation errors in bistatic L-band staring radar is found in ref. [23], these were corrected using a method exploiting the direct signal from the transmitter, provided that there is a direct line of sight. This is revisited and extended in this paper to enable synchronisation capability without requirement of a direct line of sight.

A review of networked radar is presented in ref. [29] which gives an overview of how synchronized networks of sensors are used in various applications, but then focuses more on the state of the art data fusion techniques. Another full review of network radars focused on detection of S-UAS targets is found in ref. [30]. Various networked radars that are developed for the purpose of drone detection are described. University College London developed NetRAD [31] which consists of

three identical transmitter and receiver nodes utilising pulsed waveforms at S-band. Successful detection and discrimination of drone targets containing various payloads was performed but demonstrated at short ranges of less than 200 m. Subsequently, NeXtRAD, a multistatic radar system for drone identification was built by the University of Cape Town and the University College London [32] and operates at both L-band and X-band. A summary of the results from both the NetRAD and NeXtRAD systems is shown in ref. [33]. Thales Singapore and Netherlands developed a different type of radar network consisting of various low cost sensors [34]. This Continuous wave (CW) K-band system was used for classification of drones against other civilian targets such as bicycles, cars and walking people. Also, multi sensor networks are available such as the radar and camera network sensor developed at Fraunhofer [35]. This sensor utilises W-band for the detection stage synchronized with a high resolution optical camera to enable the operator to classify the target.

The central problem being addressed in this paper is the surveillance of drones in an urban environment. These environments bring additional complications such as significantly increased clutter, multipath, additional interference sources and target obscuration due to large buildings. Networked radar systems are used to mitigate some of these challenges. It can be seen in the literature, there are various other established radar networks but few truly capable of detection of S-UAS targets at useful ranges and few operating in urban environments. In addition, synchronisation is typically achieved using a network time protocol (NTP), white rabbit protocol [36] or GPS disciplined oscillators (GPSDOs) [37] which all either require additional infrastructure, are vulnerable to GNSS spoofing or limited in the precision and accuracy. The approach used in this work is a relatively low cost, direct signal synchronisation technique. This does not require any direct links to be built between the radar nodes nor does it rely on GNSS signals. The synchronisation performance is not expected to be as high as the other techniques but can be a viable, low cost alternative. It should be noted that the concept has been used extensively for the use in passive radar where a separate antenna is used to collect the direct signal for matched filtering [38]. It has been used as early as the 1940s in the Klein Heidelberg network where transmission from the UK home chain system was used as a signal of opportunity [39]. Modern passive radar systems continue to use the direct signal breakthrough with other communication type signals such as DVB [40], WiFi [41] and GNSS [33, 42]. Upcoming sensors are looking into using 5G [43] or Starlink [44]-based passive radar systems. It is common with all of these passive sensors that the transmitter is uncooperative and therefore, detection of the direct breakthrough signal is required. In this work, where the transmitter is cooperative, the waveform properties are already known. The direct breakthrough signal is not necessarily required for synchronisation if there are other reference points available such as direct signal returns from large structures. At the University of Birmingham, a network sensor, Advanced Radar Network (ADRAN), is being developed. This overlooks the Birmingham city region [11, 17, 18]. The work presented in this paper demonstrates one of the first examples of L-band

network radar measurement of S-UAS targets in a cluttered urban environment.

The rest of the paper is organised as follows. Section 2 explains the effect of synchronisation errors in a radar network and section 3 describes the steps for processing the data and performing synchronisation via the direct signal. Section 4 describes the simulation model developed and presents the results containing low radar cross section (RCS) targets. Section 5 explains the radar configuration used for collecting the data and section 6 shows the results of drone detection using the L-band bistatic staring array radar. In this way the processing methods on real data are validated. Finally, conclusions are drawn in section 7.

2 | EFFECT OF TIMING AND FREQUENCY ERRORS IN AN L-BAND RADAR NETWORK

There are two aspects that are required in network operation relating to synchronisation, (i) the timing of pulse transmission and (ii) frequency coherence. In a monostatic radar, at relatively shorter ranges, synchronisation is naturally achieved since the local oscillator is shared between transmitter and receiver, and the noise is common on both. The simulations and experiments in the paper utilise a pair of radars that are spatially separated, with no dedicated communications link and are both operating with a separate local oscillator and therefore, time and frequency synchronisation cannot be assumed. A lack of time synchronisation means that the receiver is unaware of the pulse sequence and subsequently the time delay and hence the range of signal returns are indeterminable. A lack of frequency synchronisation will result in an overall Doppler offset in the return signal and then issues in converting down to baseband, due to the incorrect intermediate frequency being generated, will also result in a buildup of timing errors [23].

The radar architecture consists of a local oscillator at frequency f_{clk} and this is the source for all of the timing within the transmitter module. To create the carrier frequency, there are several methods by which this can be achieved, such as, using a phase lock loop (PLL) upconversion [45, 46], direct digital synthesis [47], using multiple frequency multiplication/mixer stages [48] or to generate the signal directly with microwave photonics [49]. To be consistent, in this work, PLL upconversion is used which generates a signal that is a multiple of f_{clk} and is also coherent. Therefore, using this technique, if the local oscillator is not stable in frequency or has an offset from its nominal frequency, the carrier frequency will also have a frequency error as denoted by Equation (1).

$$\Delta f_c = N\Delta f_{clk} \quad (1)$$

where N is the PLL upconversion factor, Δf_{clk} is the frequency error of the local oscillator and Δf_c is the frequency error of the transmitted carrier signal [23]. Typically N , in a PLL architecture, can vary from 10 to 100, which demonstrates the importance of the frequency stability of the radar's local oscillator.

For a network radar, the timing of the transmit waveform is based on the local oscillator in the transmitter node and the timing of the sampling of the incoming echos are derived from the local oscillator in the receiver node. If there is a discrepancy between the frequency of both oscillators, a timing error will build up in the radars. For example, if both radars have separate crystal oscillators that start with the same nominal frequency but are then left to be free running, then they will still have uncommon frequency fluctuations due to the random nature of individual oscillators. This can cause a 'random walk' of the timing error. Also, the crystal oscillators will have a frequency drift due to the ageing of the crystal and temperature variations causing a potential systematic frequency offset between the two. The result of this is a timing offset that can continuously become larger and larger. In terms of radar performance, the timing offset results in an error in the bistatic range measurement (ΔR_B) and is determined by Equation (2).

$$\Delta R_B = c\Delta t \quad (2)$$

Where c is the speed of light in free space and Δt is the timing error which can range from 0 up to an entire pulse repetition interval (PRI). For radar networks, it is also important to note that the receiver architecture uses antennas that are non-co-located with the transmitter. The incoming signal is mixed down to the intermediate frequency (IF), digitised with the analogue to digital converter (ADC) and the waveform is processed by a matched filter. If the receiver LO frequency is different, the baseband mixing frequency and therefore both the IF and ADC sampling frequency will be different. Also, since the matched filter is predefined, this will not match the frequency of the waveform. The combination of these effects leads to the inability for the radar to correctly mix down the signal to baseband. In section 4, this is shown to produce a shift in the frequency domain when the magnitude of the difference in frequency is greater than the Doppler frequency resolution.

As mentioned previously, the timing error results in a range error. In digitised baseband data, this appears as an equivalent offset in the range dimension. This growing range offset causes a movement in the range dimension over time or a 'range drift'. After signal processing, this range drift makes stationary clutter appear to be moving either towards or away from the radar depending on the sign of the frequency offset. Overall, range drift is a secondary effect of the frequency offset. To make things worse, most radars will only be recording the received signal for a fraction of the PRI. Under these conditions, useful information can drift into the regions of the pulse cycle that are not being recorded and will be lost.

3 | PROCESSING

In order to understand the impact of the lack of synchronisation just described, the form of the range-Doppler data can be examined. The steps used to generate range-Doppler data as part of the monostatic processing chain is as follows. The

radar records the ADC output for all 64 channels and performs the matched filter to obtain in-phase and quadrature components (IQ) at baseband. The IQ data for all 64 receive elements are saved to a hard disk internal to the radar. Range Doppler plots are generated by transforming the time domain, pulse by pulse data, into the frequency domain by performing an FFT with a Blackman-Harris window. Digital beamforming is then used to select the desired azimuth and elevation angles where all channels are phase shifted and subsequently combined. This range-Doppler data is generated for each consecutive coherent processing interval (CPI), set at 0.5s. The range swath is 0.3–5 km for the standard monostatic setup and the pulse repetition frequency (PRF) is fixed at 7.5 kHz, leading to a Doppler frequency span of -3.25 kHz to $+3.25$ kHz at baseband. At this stage, the spectral data is obtained for a single CPI contained within a 4 dimensional array with dimensions of azimuth angle, elevation angle, range bin and Doppler frequency bin.

The next step involves determination of the background levels. To obtain the background noise levels, the process is repeated to obtain the spectral domain data for each consecutive time step over a specified period. For each of the beams, range bins and Doppler frequency bins, the spectral data for each CPI over the specified period is averaged and this value represents the background level within that particular resolution cell. To reduce the influence of moving targets, only every M th frame is considered for a total of N contributions. N is sufficiently large so that if a target is present, it will only be in the same resolution cell for a small percentage of the total time interval. The 4-dimensional array, now containing time averaged values of the spectral domain data is now termed as a spectral background map (SBM). As the background may change over time, the SBM is regenerated every 10 min.

Target spectrograms are generated for controlled drone flights and therefore, have the advantage of truth data availability. Truth data, extracted using the flight information from controlled drones is used to aid with the range gate and beam selection and then the spectral domain data for each time step is appended to the spectrogram. The SBM cells matching those contained in the spectrogram are subtracted from the spectrogram itself so that the targets presence is enhanced through the noise.

3.1 | Bistatic data processing

For bistatic radar, there is an inherent lack of synchronisation between the radars. A processing sub-chain for synchronising the bistatic data with the direct breakthrough signal has been devised to solve this issue in [23]. After performing this software correction, the data can be processed in an identical manner to the monostatic data. The bistatic data correction can be broken into 3 steps, (i) detection of the direct breakthrough signal from the transmitter, (ii) correction of the frequency offset, and (iii) correction of the range offset. Improvements to the method presented in ref. [23] include, range profile correlation for more accurate detection of the

direct breakthrough signals peak position, sub-CPI frequency shifting and SBM processing.

Firstly in the matched filtered data, there is an estimation of the range and Doppler cell containing the direct signal. Previous methods involved interrogating the range-Doppler data and looking for the transition between range bins containing thermal noise and when they contain signal + thermal noise [23]. Due to the lower range resolution of the radar, sometimes it is difficult to extract the peak of the direct signal as it is mixed with other large returns close to the receiver. Therefore a new method is used here where the entire clutter profile, is used to calibrate the timing of the radar using a range profile correlation method. A range profile reference is generated by using an average of the clutter profile over an extended period of 3 min, where the direct signal is detected using the original method [23]. Additional benefit is gained by oversampling both the current range profile and the reference range profile so that the direct signal is estimated beyond the range resolution limits of the radar. Cross correlation is performed to determine the range containing the direct signal. An example is shown in Figure 1, where the incoming range profile is matched with significant features of the reference range profile via correlation.

For the frequency offset correction, the clock frequency offset is calculated by its deviation from the zero Doppler frequency. With this, the frequency correction is applied by using a constant added frequency which is equivalent to a linearly increasing phase shift. First order clock drift is then added via a quadratic increasing phase shift as in equation (3).

$$y[n] = x[n]e^{-i2\pi\left(\frac{f_0 n}{PRF} + \frac{f_1 n^2}{PRF^2}\right)} \quad (3)$$

Where $y[n]$ and $x[n]$ are the pulse samples before and after correction respectively and n is the time step index. While

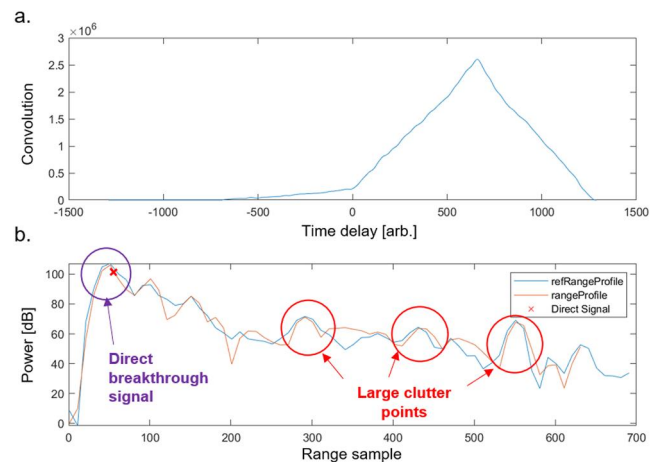


FIGURE 1 Example of range profile correlation method for estimation of the range misalignment (a) result of the correlation and (b) comparison of range profile after performing the range offset correction to the reference range profile. This can be used to determine the location of the direct breakthrough signal in the misaligned data.

f_0 and f_1 are the frequency offset and frequency drift parameters respectively. This is an extension of the equation used in [23] but with a linear drift factor to obtain sub-CPI frequency correction for when using oscillators with linear drift characteristics such as oven controlled crystal oscillators (OCXOs).

Finally, for the range correction, The range offset (δt) is determined by using the expected and observed location of the direct signal as shown in Equation (4).

$$\delta t = t_a + t_b - t_c \quad (4)$$

Where t_a is the blanking time, t_b is the time between the start of the sampling window and the direct signal, t_c is the time delay before the direct signal is found in the receiver. The updated range gates are then defined as in Equation (5).

$$t_r^{2,1} = t_1^2 + \delta t + (r-1)t_g \quad (5)$$

$$t_r^{n,m} = t_1^n + \delta t + (r-1)t_g \quad (6)$$

This can be extended to a network of any number of receivers as shown in Figure 2. Where t_r^n is the local time of the r th range gate for radar n and $t_r^{n,m}$ is the updated local time of radar n , where transmitter radar m is used for the synchronisation correction and t_g is the time interval per range gate. After the correction of the frequency and timing offsets in the bistatic data, it is modified into the same data format as the monostatic raw data and sent to the rest of the processing chain.

3.2 | Signal processing chain for target detection

The full signal processing chain is shown in Figure 3 where the green highlighted blocks are unique to the data from the

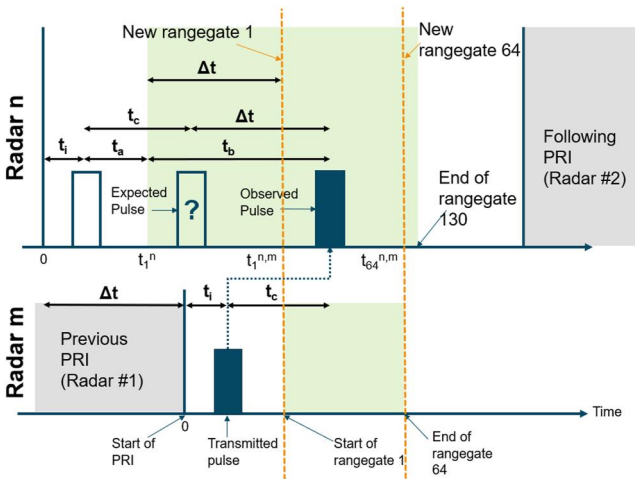


FIGURE 2 Timing diagram for correcting the range offset using the direct signal in a pulsed bistatic radar. The bottom timeline represents the transmitting radar while the top timeline shows the receiving node. By identifying the difference between the expected and the observed pulse position, the range offset can be corrected.

bistatic radar where the bistatic corrections are applied. For monostatic processing, these steps are skipped.

Raw radar data was processed offline to generate SBMs as described earlier. The next stage reads the raw data frame and then if the data is bistatic, direct signal detection, frequency offset correction and range correction are performed as described in the previous section. The first stage of beamforming is then applied by using a grid of preselected beams that are matched with the SBM. The SBM is used as a cell averaging CFAR for the detections processing where for each cell under test (CUT), the equivalent cell in the SBM, which consists of the average value of the window cells taken in the temporal dimension, is then subtracted from the CUT and then subsequently a set threshold is applied before making an initial decision on if the CUT contains a target. Next, there is a detection filtering stage where all earmarked detections occupying both a common range and Doppler frequency bin are compared and all but the strongest SNR quantity are removed. The staring radars course azimuth resolution and the process of beam selection can cause duplicate detection where the same target appears in different beams. This stage ensures duplicate detections are removed before further refinement.

The filtered detections are then refined for angle and range. Firstly, the azimuth and elevation angles are improved with another beamforming stage with finer grid spacing. Quadratic interpolation is used to improve the range estimate. If the detections are using a bistatic geometry, the bistatic range is converted to the range between the receiver and the target using trigonometry as in Equation (7) [50, 51].

$$R_R = \frac{R_B^2 - L^2}{2(R_B - L \cos \theta)} \quad (7)$$

$$R_B = R_T + R_R \quad (8)$$

Where R_B is the bistatic range as calculated due to the time of signal time of flight from the bistatic node, L is the baseline distance between the two radars, θ is the angle between the vector connecting the baseline and the vector connecting the receiver to the target, R_R and R_T are the ranges to the target from the receiver and transmitter respectively. With the refined azimuth and elevation angles as well as the range, a coordinate transformation is performed to determine the target location in the local Cartesian and geodetic coordinate systems.

Then, there is an additional stage of filtering detections when the target falls outside the feasible FOV. The final stages of the signal processing are target tracking and classification but are not fully explored within this work. However, detections corresponding to the controlled drone target are extracted manually with the aid of the flight truth data where the detections are restricted by position and velocity. A smoothing filter is then applied to give an indication as to the final tracking performance of the bistatic radar.

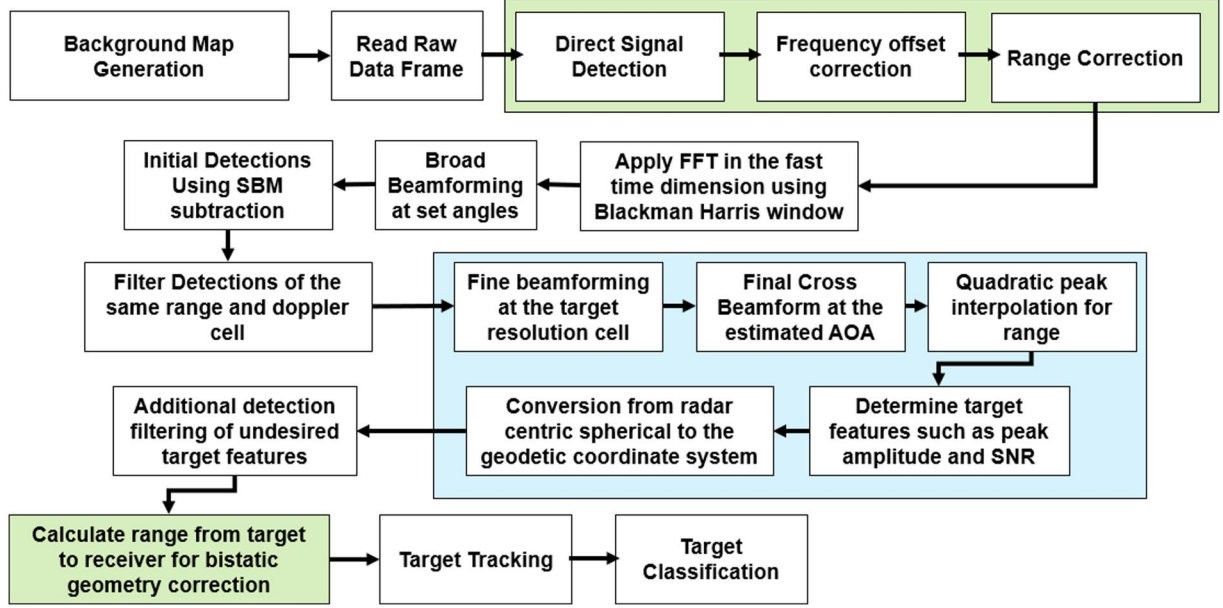


FIGURE 3 Signal processing chain for bistatic synchronisation, detection, tracking and classification of targets.

4 | BISTATIC RADAR SIMULATIONS

Simulations have been developed to model the effect of the timing and frequency offsets on an L-band staring radar network and to verify the proposed method for bistatic correction via direct signal synchronisation. The simulation is able to emulate a network consisting of multiple radar nodes, the effect of the local oscillator on network synchronisation and to produce radar outputs with multiple moving targets and clutter. The simulations assumes a staring array radar as previously described in refs. [11, 17, 18].

This section describes the radar simulations for the bistatic geometries in an urban like environment. Several assumptions and simplifications are made to allow echo data to be generated in reasonable time. Since the staring radar transmits a wide beam, the assumption that the beam power is independent of angle from the boresight is made. All targets and clutter are modelled as point sources. To further simplify the modelling, it is assumed that the phase noise contribution is only due to the oscillator phase variations in the transmitter, so no additional noise is added to the receiver and there are no ADC time errors. The objective of the simulations is to examine the effect of the non-fully coherent clocks on a radar network. The running of the simulation can be split into 5 sections; (i) setting up the radar environment, (ii) generating the signal at the receiver, (iii) internal hardware processing, (iv) updating the timing parameters and (v) the signal processing after digitisation. A block diagram of the simulation is shown schematically in Figure 4.

4.1 | Simulation methods

Initial setting up of the radar environment entails setting the position of each of the radars, the parameters of each internal

oscillator and setting each target and clutter with their own internal properties. Each oscillator has a phase walk parameter $d\phi$ which defines the variance of a Gaussian distribution used to apply a phase jump at each time step. The oscillator is also given an initial time offset from the reference node t_0 , initial frequency offset from the reference node f_0 , and coefficient for linear frequency drift of the oscillator f_1 , which will relate to the synchronisation of the radar network via the timing errors accumulated between the respective oscillators of the network. The targets will have an initial position, constant velocity vector and RCS. The clutter will also have a set position, and RCS. Each radar used in this simulation has a 16 by 4 array of digitised receive elements placed in a rectangular grid pattern and element spacing equivalent to half a wavelength. This replicates the array set-up in the L-band radars used in the experiments. The transmit waveform is a single pulse, identical to the staring radar used in the experimental work, and resembles a rounded rectangular pulse, as seen in Figure 5a. The pulse has a central frequency of f_c . In the simulations current form, the signal is generated at the carrier frequency as it reaches the staring radar receiver. The signal at receiver n is modelled as shown in Equation (9).

$$y(t) = \sum_{r=1:R} \left[d_r(t) + \sum_{n=1:N} t_n(t) + \sum_{m=1:M} c_m(t) \right] + w(t) \quad (9)$$

Where $d_r(t)$ represents the direct signal from transmitter r , the second component is the echo return from N targets, the third component is from M clutter points. Finally, $w(t)$ is the thermal noise added after summation of the signals from all R radar transmitters. The direct signal, clutter and targets are modelled in a similar way and an example of a single target return is shown in Equation (10).

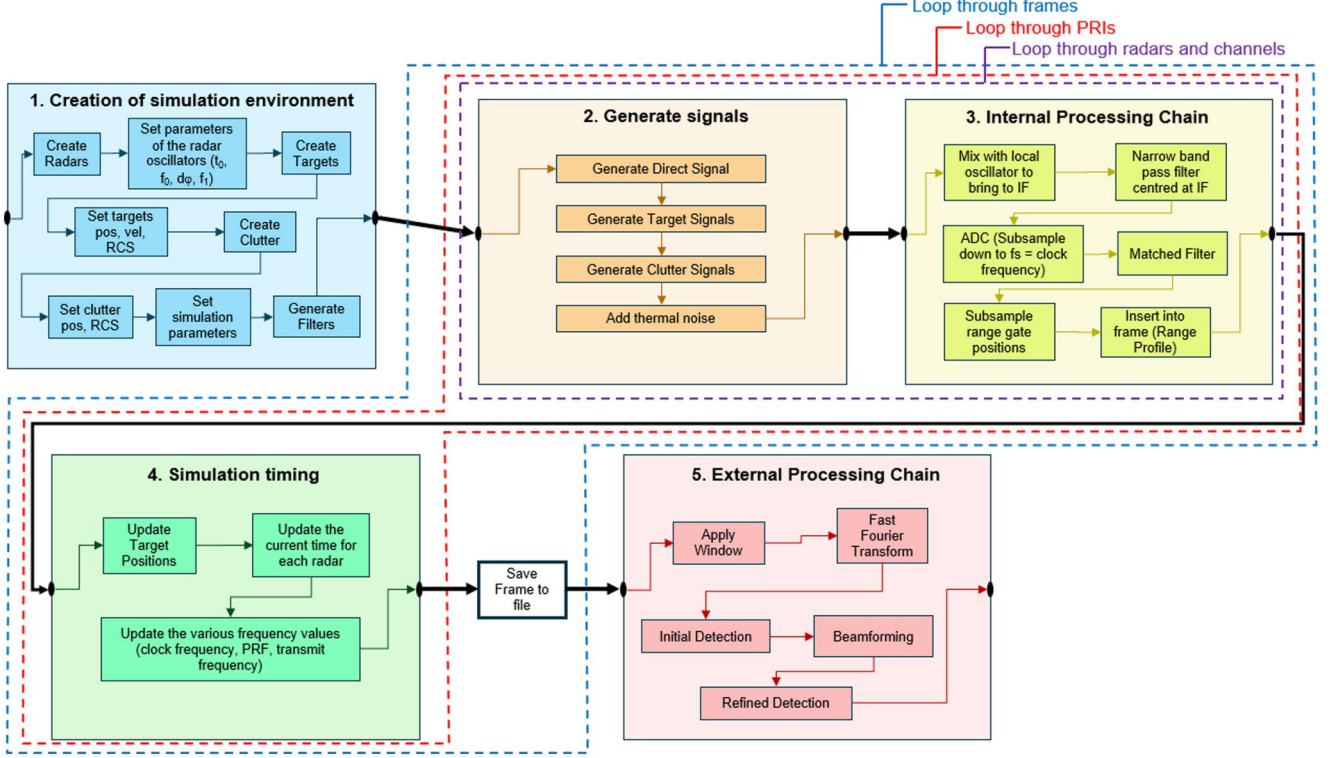


FIGURE 4 Block diagram showing the 5 components of the simulation: simulation environment setup, signal generation, internal processing, simulation timing and the digital signal processing.

$$t_n(t) = E(t)Ae^{i2\pi f_{c,n}(t-\tau)+\phi(t)} \quad (10)$$

$$\Delta T(t) = t_o + (f_0 t + f_1 t^2)/f_{nominal} + \epsilon(t) \quad (13)$$

$$A = \sqrt{\frac{P_{tx}\sigma\lambda^2 G_T G_R}{R_T^2 R_R^2 (4\pi)^3}} \quad (11)$$

Where $E(t)$ is the pulse envelope, $f_{c,n}$ is the instantaneous carrier frequency of the n th transmitter, τ is the time delay of the signal propagation through free space. Also, P_{tx} is the power of the transmitter, σ is the RCS of the target or clutter, λ is the wavelength of the carrier. G_t and G_r are the antenna gains of the transmitter and receiver respectively. The effect of the oscillator frequency stability is provided by the time variant phase offset $\phi(t)$, shown in Equation (12).

$$\phi(t) = \phi(t - t_s) + N(0, d\phi) + t^2 f_1 \quad (12)$$

Where the first component demonstrates the time variant behaviour of the equation by extracting the phase at a previous time and t_s is the sampling interval used in the simulation. The second component is the phase walk that is applied to the signal using a random normal distribution with a mean of zero and variance of $d\phi$ and this represents the effect of random walk phase noise in the radar. The third component is the linear frequency drift of the oscillator. By using the expression for time error of oscillators [52], the relative time error ΔT at a time t of the transmitter node from the receiver node can be represented as a function of time with Equation (13).

The final term $\epsilon(t)$, represents the additional time error from the random phase walk.

After signal generation at the receiver, the internal hardware is simulated to mimic closely the staring radars used experimentally. The first stage is mixing the signal down to the intermediate frequency using a CW signal at frequency $f_{c,n} + f_{IF,n}$. The signal at this stage is shown in Figure 5c. Next there is a band-pass filter with a pass band of 20 MHz to extract only the spectrum around the IF frequency. The next stage is the ADC, this has been implemented as a sub-sampling of the data since up to this stage, the signal had a sampling frequency that is an integer multiple of the clock frequency used for the ADC. Time and frequency representation of the ADC output is shown in Figure 5d–e. Next, the matched filter is applied to the ADC output by cross-correlation with the expected return at this stage as shown in Figure 5f and then the signal is sub-sampled again to define the range gates. This internal processing chain will repeat for each pulse cycle until a full data frame has been build up consisting of 2048 pulses.

For each PRI, the local time at each oscillator is updated. Since the oscillator signal is not common at each node, there is potentially a defined time and frequency offset. The clock frequency (f_{LO}) of each radar is updated with Equation (14) where the nominal frequency $f_{nominal}$ is offset by the initial offset frequency and a linear frequency drift correction is applied. The value of f_{LO} then defines both the PRI and f_c so these are also updated for each radar in Equation (15) and

Equation (16) where N_{cycles} and N_{PLL} are the number of clock cycles in a pulse interval and the PLL up-conversion multiplier to f_c respectively. These are both constant and set in the

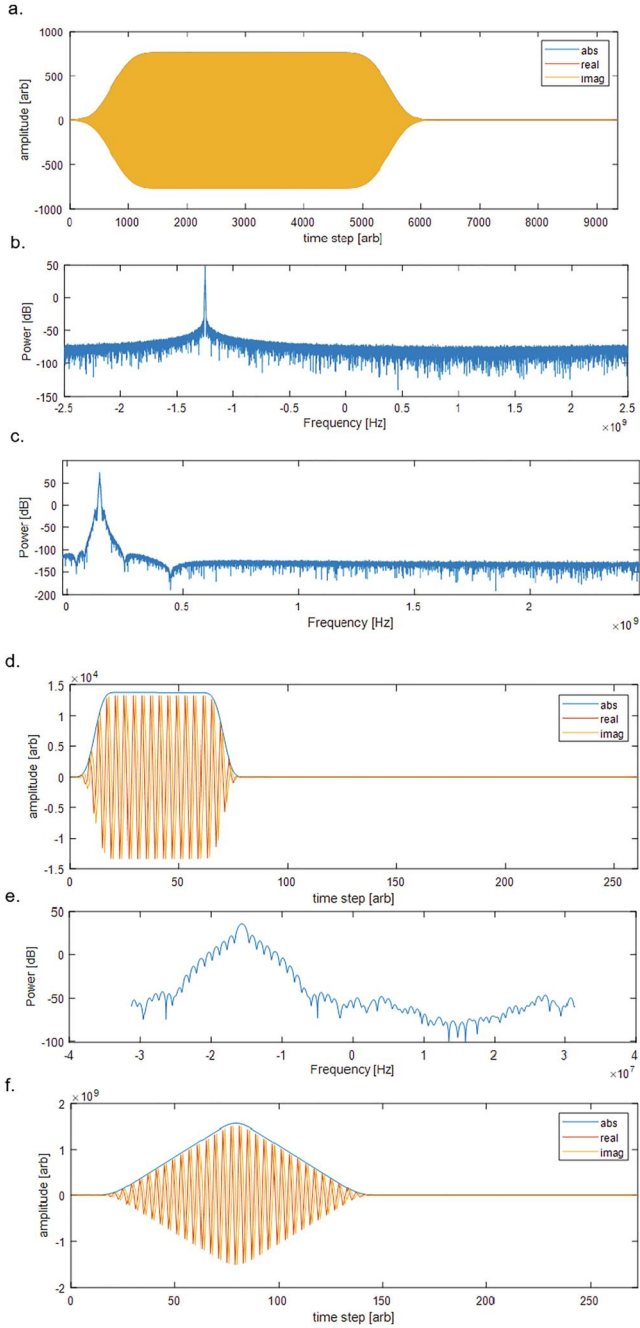


FIGURE 5 Signal at various points within the internal processing chain. (a) Initial received pulse in time domain, (b) received pulse spectrum, (c) spectrum after mixing down to IF, (d) time domain signal after ADC, (e) ADC output spectrum, and (f) Matched filter output.

simulation parameters. The local time of each radar is then updated in Equation (17) using the PRI of the same radar. The target parameters are also updated using the timing properties of the oscillator within the receiver radar node. Upon completion of all 2048 pulses, the data frame is assembled and the same digital signal processing chain as in section 3 is used. This describes the simulation of the radar output in the temporal domain from the voltage signal at the receiver to the matched filtered output. The data format is identical to that of the real raw data in the experimental staring radar and therefore, the data is used interchangeably within the processing tools to generate equivalent outputs.

$$f_{LO}(t) = f_{nominal} + f_0 + tf_1 \quad (14)$$

$$f_{PRF}(t) = \frac{f_{LO}(t)}{N_{cycles}} \quad (15)$$

$$f_c(t) = N_{PLL}f_{LO}(t) \quad (16)$$

$$t[p] = t[p - 1] + PRI[p - 1] \quad (17)$$

4.2 | Simulation results

This section describes the simulation results for a scenario that mimics an urban environment similar to the radar network on campus in Birmingham. The simulation is setup to contain 3 targets, the parameters are shown in Table 1. To represent the urban environment, 33 clutter points are added as this is sufficient to fill the radar FOV with stationary returns. Each clutter component is placed away from the origin by ranges increasing by 150 m, each is assigned with a constant RCS value as shown in Figure 6a and they are placed at a different azimuth angle from boresight as shown in Figure 6b. In the first iteration, a single monostatic radar (radar A) is placed at the origin and the full simulation environment is shown in Figure 7.

A total of 64 receive elements are used in a 16×4 grid pattern with an element spacing of half a wavelength and the simulation was run to generate echo data for 2048 pulses. The oscillator was given a phase walk parameter of $2e-5$ and a linear frequency drift of $1e-5$ Hz/s. The processing used on the data is as described in previous sections. The output of the simulation is translated into the range-Doppler domain for the beam at 90° azimuth and elevation and is shown in Figure 8. Targets 1 and 2 are clearly visible on the range-Doppler map in range gates 5 and 12 respectively. Target 3 is weaker in power (due to the direction of the beam) but is shown in range gate 50. The digitised IQ data from all 64 elements in the receive

Number	Position [m] (x, y, z)	Velocity [m/s] (x, y, z)	RCS [dBsm]
Target 1	(0, 500, 0)	(0, 10, 0)	-30
Target 2	(342, 940, 0)	(0, 10, 0)	-30
Target 3	(1690, 3625, 0)	(0, 10, 0)	-30

TABLE 1 Initial target states for simulation iteration 1. Monostatic urban scenario.

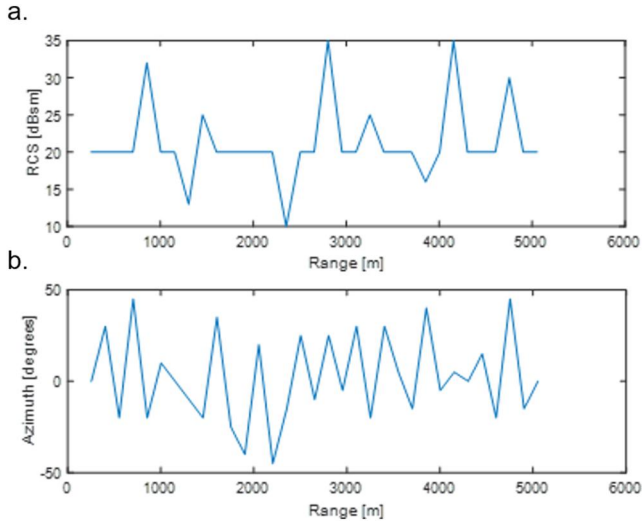


FIGURE 6 Parameters used for the clutter points used within the simulation. (a) RCS values of the clutter and (b) Azimuth angles of the clutter.

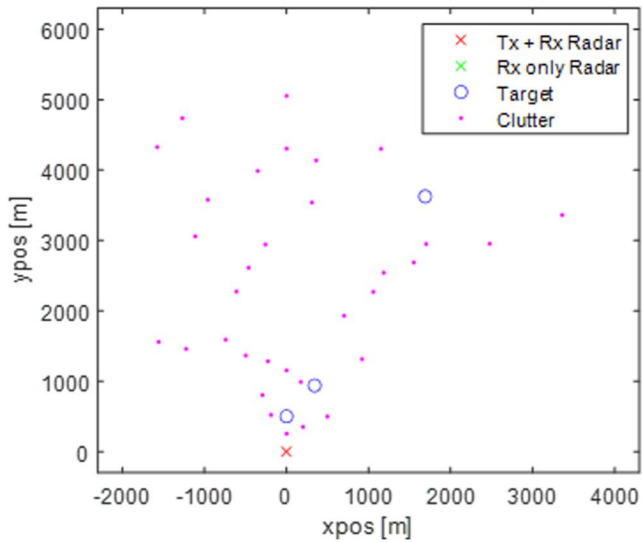


FIGURE 7 Radar Environment for the monostatic simulation. This scenario contains no Rx only radars, 3 targets and 33 clutter.

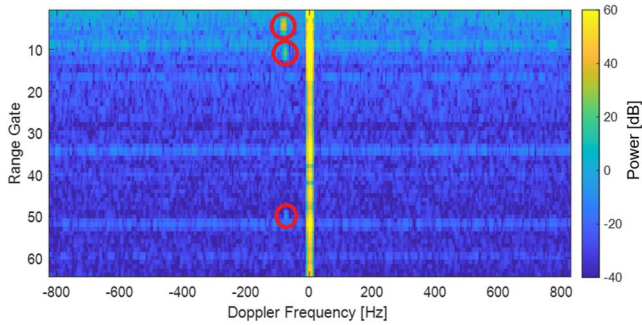


FIGURE 8 Range Doppler plot of simulation 1 for the broadside beam, showing three targets at varying ranges, circled in red.

array are available within the simulation so digital beamforming can be applied to determine the angle of arrival (AOA). The beam profile for each of the three targets can be seen in Figure 9. In the beam profile of target 3, there is a node close to the broadside angle which explains the weaker signal power in Figure 8. With the range and the AOA available, the target can be localised in 3D Cartesian coordinate system and the results are presented in Table 2. The positional error of the three targets respectively are 0.7 , 13.1 and 74.2 m and the measured SNR of the three targets are 48.5 dB, 46.4 and 42.1 dB respectively.

The second iteration of simulations use the same setup of clutter and targets but will instead incorporate a second radar node (radar B) that is placed at [-1000, -1000, 0]m and data is generated for only the output of (radar A) which is still located at the origin but transmits no signal. A 2-D plot of the radar environment with the locations of each clutter and target is seen in Figure 10. Since radar B is not transmitting, echoes originate from the second radar only, to simulate bistatic operation. For the oscillator variables, the phase walk and linear frequency drift parameters are set to the same values as the previous simulation (2e-5 and 1e-5 Hz/s respectively). The frequency offset of the local oscillator for radar B (the transmitting radar) is set to -20 Hz and the timing offset for radar B is set to 10% of a PRI. Radar A is set to record 130 range gates rather than 64 in order to capture a larger proportion of the recording window of interest. Once again, the simulation is run for a single frame containing 2048 pulses and the IQ data

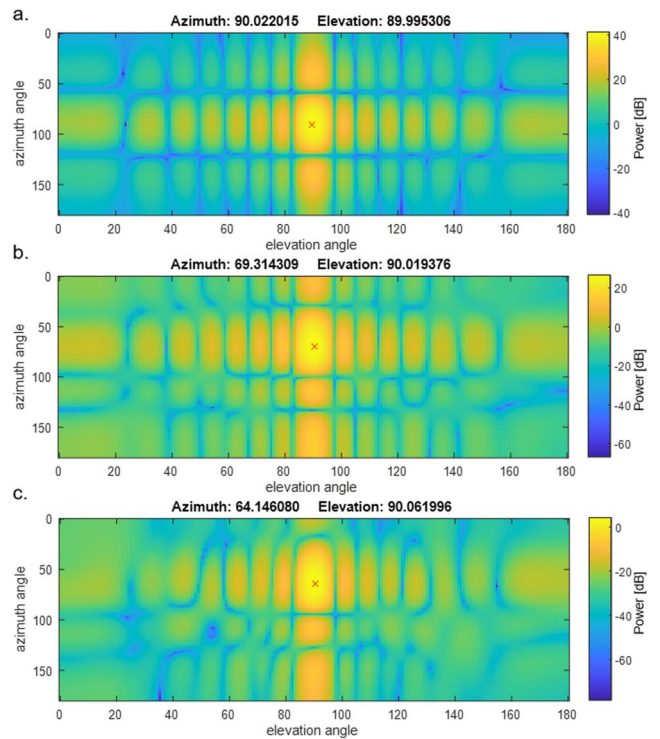


FIGURE 9 Beam profile of each of the 3 targets where the red cross shows the measured AOA of the target. (a) Target 1, (b) target 2, and (c) target 3.

Number	Position [m] (x, y, z)	Range rate [ms ⁻¹]	Positional error [m]	SNR [dB]
Target 1	(-0.2, 499.3, 0)	-9.9	0.7	48.5
Target 2	(355.0, 938.1, 0.2)	-9.5	13.1	46.4
Target 3	(1758.5, 3593.2, 1.3)	-9.1	74.2	42.1

TABLE 2 Monostatic simulation results.

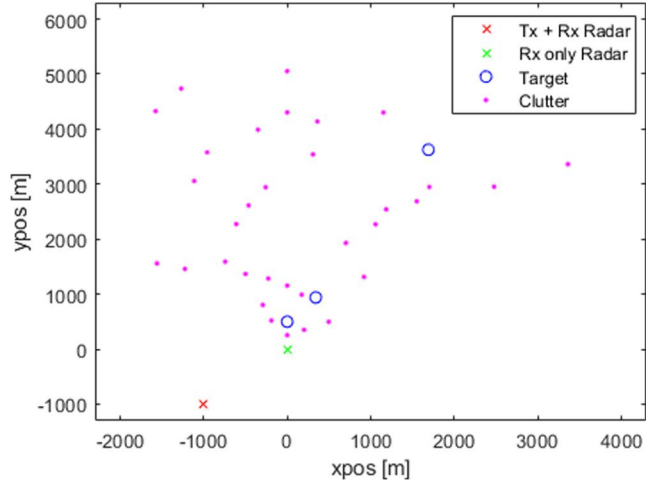


FIGURE 10 Radar Environment for the bistatic simulation with one receive only radar, 3 targets and 33 clutter.

is recorded for all 64 elements on the receive array. After converting the resulting data to the range-Doppler domain, the results are seen in Figure 11a. It is observed that the timing offset causes the entire range profile to change as the unsynchronized receiver is not sufficiently aware of when the pulse is emitted from the transmitter. Also, the frequency offset causes the entire spectrum to shift by a certain amount. The reason for this is the carrier frequency of the two radars are now also different according to Equation (16) and the radar is no longer able to successfully mix the received signals down to baseband. In this example, all of the stationary clutter appears to have a Doppler frequency of -400 Hz which is equivalent to a target moving at 48 m/s. The timing error observed is 13.6 μ s, matching the simulation input parameters.

To proceed, a bistatic data correction method is applied to the data to locate the direct signal, correct the frequency offset and correct the range offset. The resulting range-Doppler plot after data correction and then transformation of the data to the range-Doppler domain is seen in Figure 11b. Here, it is clear to see that the range has been shifted and the stationary clutter now appears at 0 Hz on the Doppler frequency axis as expected. Again, three targets are seen within the data at range gates 13, 20 and 58 respectively, which is consistent with where the targets are expected but note that this represents the bistatic range before performing the appropriate geometrical conversion. Again, after using the detected bistatic range and digital beamforming to obtain the AOA, the 3 targets can be localised in 3 dimensions. The targets are able to be detected near to the expected locations as seen in Table 3 and the positional errors of each of the three targets are 6.3 , 12.2 and 30.3 m respectively. The SNR of the targets in the bistatic case

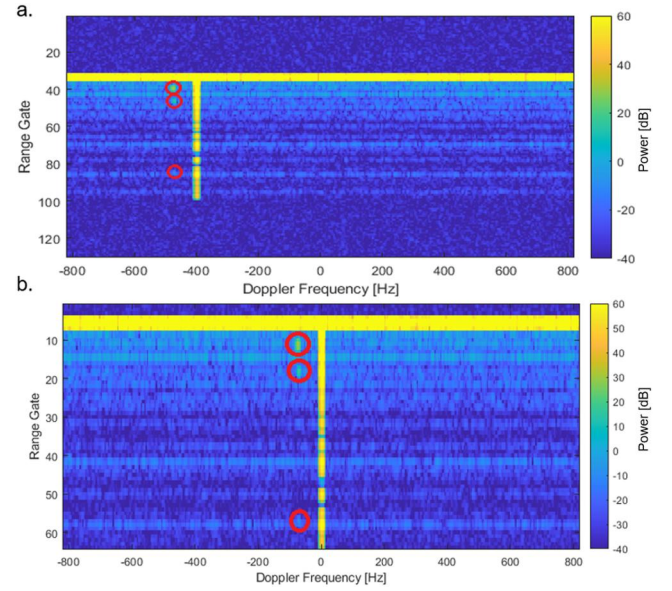


FIGURE 11 Initial Range Doppler plot of simulation 2 with the controlled drone target circled in red (a) before bistatic corrections and (b) after applying bistatic correction and the targets are appearing in the predicted resolution cells.

is reduced, by 7.3 dB, 7.5 and 16.1 dB for the 3 targets respectively, this is partially due to the longer travel time and attenuation due to the position of the transmitter.

In addition, the detection information from the two radars can be combined using data fusion techniques. This work does not look into this in detail but a simple averaging of the position can be used to potentially reduce the positional error in comparison to a single radar. When averaging the position, the positional error becomes 2.9 , 12.7 and 52.5 m respectively. Overall the results from the simulation are able to demonstrate effects of frequency error, timing error and phase noise on the radar output. This simulation has also provided the means to validate the functionality of the bistatic synchronisation correction via direct signal. The correct target position was successfully extracted from the data with time error. In some cases this gives a more accurate position than the monostatic radar alone.

5 | EXPERIMENTAL TRIALS SET-UP WITH STARING RADAR

In this section, the configuration for the experimental field trials with the two L-band staring radars at the University of Birmingham will be described. The two radars are near identical commercial of the shelf (COTS) systems, with the main difference being they have different local oscillators and a

TABLE 3 Bistatic simulation results.

Number	Position [m] (x, y, z)	Range rate [ms^{-1}]	Positional Error [m]	SNR [dB]
Target 1	(-1.3, 506.2, 0)	-9.1	6.3	41.2
Target 2	(354.2, 939.3, 0.3)	-9.1	12.2	38.9
Target 3	(1719.0, 3613.4, -0.7)	-9.1	30.3	26.0



FIGURE 12 ADRAN facility at the University of Birmingham showing the two L-band staring radar systems. Radar #1 (right) and Radar #2 (Left)

slightly different transmit power. Therefore, this needs to be accounted for when making direct comparisons between the two systems. Otherwise, waveform and all other characteristics and the signal processing are the same for both radars. A pulsed waveform at frequency f_c and a PRF of 7.5 kHz is used with a total integration time of approximately 0.5s.

The radar trials in this work focus on operating the radars in a non-coherent network configuration with no direct synchronisation between the two nodes. The two radars are located on two rooftops at the University of Birmingham and have a baseline distance of 188 m as shown in Figure 12. The FOV of the two radars are mostly overlapping and the trial sites have been chosen so that the controlled target can be simultaneously observed by both radars and with a varying bistatic angle. The radars are referred to as Radar #1 (located on UoB building named Gisbert Kapp) and Radar #2 (located on UoB building named ERI) for simplicity. The trial consisted of 3 controlled drones, ranging from the lower average RCS, DJI mini mavic 2 to the larger DJI Inspire 3. Also some flights were taken with the DJI mavic 3 which would have an intermediate average RCS comparatively. The DJI Inspire 3 was programmed to fly in autopilot mode to follow a set of pre-defined waypoints. The other drones did not have this inbuilt capability and were instead flown manually through the same waypoints. During the trials, a scenario named 'Richmond' was used, which had a start and end point and five other waypoints throughout the path and those waypoints are shown in Figure 13. For each flight, one of the radars (Radar #1) was operated in standard monostatic mode while the other (Radar #2) was running the bistatic/receive only mode. Due to the non-coherent nature of the radars, the synchronisation was performed in processing as described in section 3.2. For the

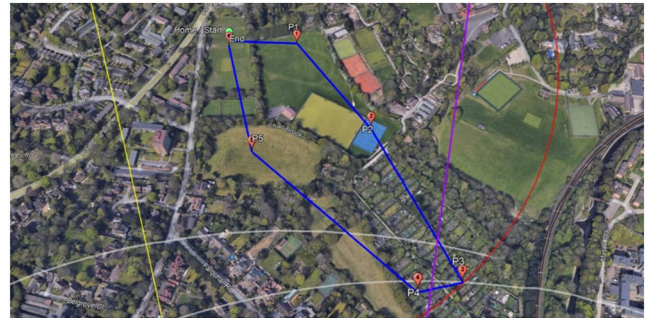


FIGURE 13 Overview of the ADRAN field trials. Drone trajectory of the Richmond scenario used in this work is marked with the blue line.

second part of the radar trials, the radar configurations were switched and Radar #2 was now the only radar transmitting. Overall, controlled drone flights were performed with 3 drones, at different altitudes (60, 80 and 100 m), both in clockwise and anticlockwise trajectories through the way points and with the two different radar configurations as described. In total, over the two days, raw radar data was recorded for both radar systems along with truth data for over 40 flights. The results described in the following section will focus on just a subset of these flights.

6 | RESULTS FROM LIVE RADAR TRIALS AND VALIDATION

This section presents the results from the field trials described in section 5. Firstly, the frequency stability of the individual radars is examined, where the individual phase noise profiles of

the transmitted signal of the two radar systems are measured. Finally, the target detection performance is analysed quantitatively using the target spectrograms and by measuring the average SNR of the drone, scaled to a constant range and comparing the detected position of the target to truth data for both the monostatic and bistatic cases.

6.1 | Phase noise measurements

At very low Doppler frequencies, either the effect of moving clutter components and Doppler processing properties such as fft size or window function would generally be the limiting factor in the radars sub clutter visibility. The frequency stability of the oscillator can start to dominate in bistatic radar systems at the low to medium frequencies since there is no correlation and thus cancelation of phase noise in the up-down conversion stages, as apparent in monostatic systems [53]. For both monostatic and bistatic radar systems the background noise level will have a fundamental thermal noise floor determined by factors such as the receiver noise figure and temperature [50]. As previously mentioned, both radar systems contain different local oscillators, each with a different type of OCXO. Here the phase noise of the OCXOs are measured within the lab environment using a Rohde & Schwarz FSWP phase noise

analyser. The signal has been measured both at f_{LO} and at f_c and the results are shown in Figure 14. Firstly, in Figure 14a the phase noise of the OCXOs is plotted and it is seen that radar #2 local oscillator has superior stability. The phase noise of the OCXO within radar #2 is lower by 10–15 dB and will result in better performance in clutter limited regions.

Within the radar, the upconversion to the carrier frequency is performed using a PLL and this would introduce additional phase noise into the system. For each of the radars, a part of the up converted signal is taken out for measurement. Figure 14b shows the phase noise of both radars at the carrier frequency and it is seen that again the phase noise is still better on radar #2, but the difference is now 5–10 dB within the range of 10–100 Hz offset frequency. This is the Doppler region where drone targets are likely to be found. It is also important to examine the frequencies beyond the maximum unambiguous frequency of the radar as aliasing effects could cause the observed phase noise in the baseband output to increase. From measurements, the far out phase noise is also lower in radar #2 but the difference is less significant. Filters included in the down conversion process are also considered and will reduce some of the high frequency noise and mitigate some of the aliasing. Spurious tones in the LO are present but are believed to be sufficiently low at less than -130 dBc/Hz. More spurs are introduced once the signal has been upconverted to the carrier frequency and are likely caused by the PLL and various electronics. These spurs in the carrier frequency are not addressed further in this work.

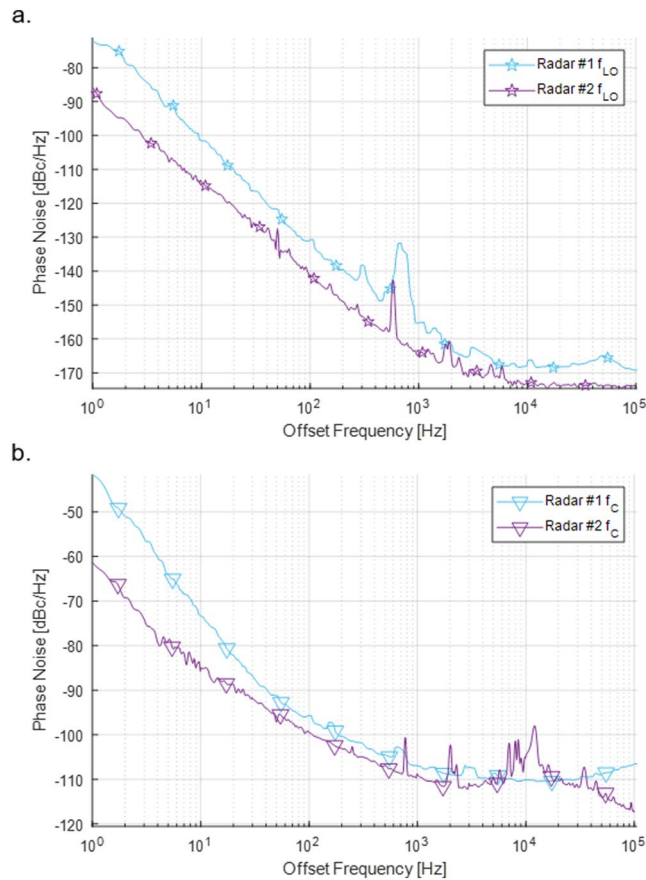


FIGURE 14 Phase noise profiles for both radar #1 and radar #2 at the (a) local oscillator frequency and (b) carrier frequency.

6.2 | Target detection performance

In section 5, the bistatic radar trials with the incoherent network were discussed. Forty controlled drone flights were performed, but here, two exemplar flights are analysed. The two selected flights use the DJI Inspire 3 drone and one is in the configuration with radar #1 as the transmitter and the other with radar #2 as the transmitter. Throughout the trial, both radars were recording raw data to the hard disk and post processing was performed. Timestamped GPS positional data was recorded on the DJI Inspire 3 using its internal real-time kinematic positioning with centimetre level accuracy which is at least an order of magnitude more accurate than is expected from radar so this GPS positioning data is a valid reference for the measurements. The range-Doppler results are also shown as well as the target spectrograms but only for the case with radar #2 as transmitter. Average SNR is also reported, along with the positional accuracy of detections compared to the GPS truth data.

Firstly, the range-Doppler data is shown in Figure 15 for a single CPI for monostatic in radar #2 and for the bistatic in radar #1 both before and after performing the bistatic correction. In the monostatic case (shown in Figure 15a), the drone target is clearly seen with high SNR of both the main body and microdoppler side bands either side. In Figure 15b, the bistatic range-Doppler for the same time step is shown and although the drone is still detectable, there is a clear error in

both frequency and range. Figure 15c shows the range-Doppler, after correction of frequency and timing errors, where the target is located correctly, according to the truth data. However, self clutter lines are evident in the bistatic range-Doppler plots that are caused due to spurs in the carrier frequency of one of the radars, these are seen at intervals of 100 Hz in the bistatic range-Doppler plots. The reason behind the self clutter lines is assumed to be due to spurs observed on the day of the trials within radar#1. In bistatic mode, there is a lack of self cancellation so the clutter lines appear to be amplified. The SBM technique for target detection mitigates the effects of the self clutter lines for preventing false alarms but the SNR of the signal is still impacted if a target enters these Doppler frequency bins. The mentioned spurs in the carrier frequency are artefacts of the radar and should not occur.

The spectrograms for the monostatic and bistatic drone flights of radars #1 and #2 were generated using the SBM subtraction technique and all four of these cases are shown in Figure 16. This shows the drone is clearly observable in all radar configurations. Since the oscillator stability of radar #2 is superior, it is no surprise that the body and microdoppler sidebands are much more apparent in the radar #2 monostatic spectrogram. The SNR of the drone body was scaled to a constant range and is shown in Table 4. There is a 9–10 dB difference between the SNR of the drone target of radar #1 and radar #2 in monostatic configuration. The reason for this is complex with various factors such as the RF transmitter power and array scan losses. These are assumed to be relatively small due to the similar transmit powers and angles from boresight. The biggest contribution in this case is expected to be due to the phase noise difference and the difference in

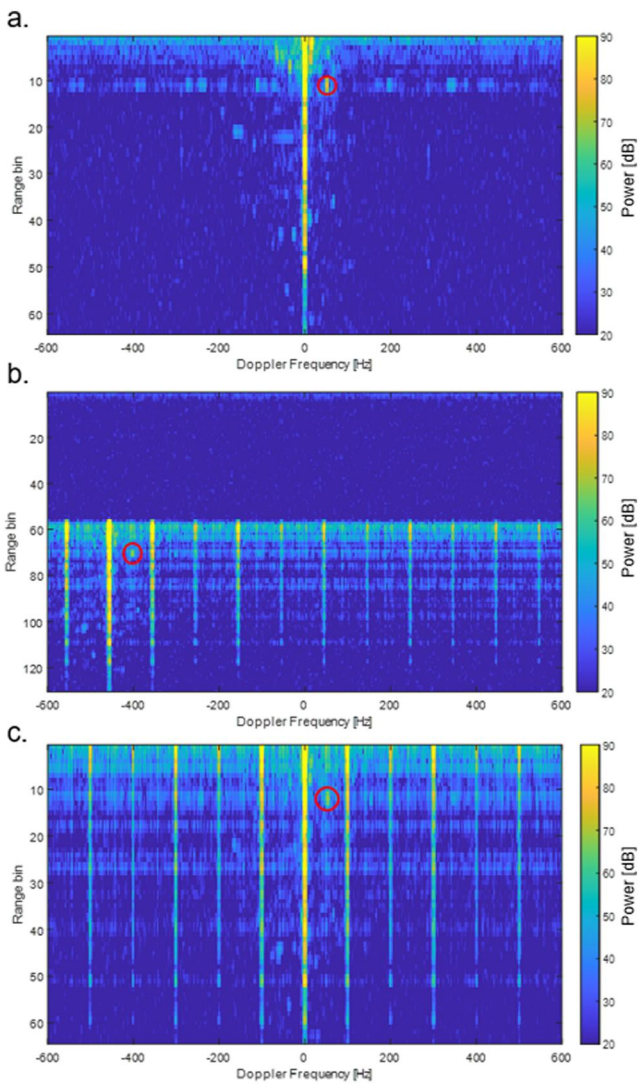


FIGURE 15 Range-Doppler plot for a single CPI during the experimental drone trials with the controlled drone target circled in red. (a) Monostatic radar #2, (b) Bistatic radar #1 before correction, and (c) Bistatic radar #1 after correction. Targets are now identified at the resolution cell corresponding to their physical location and range rate.

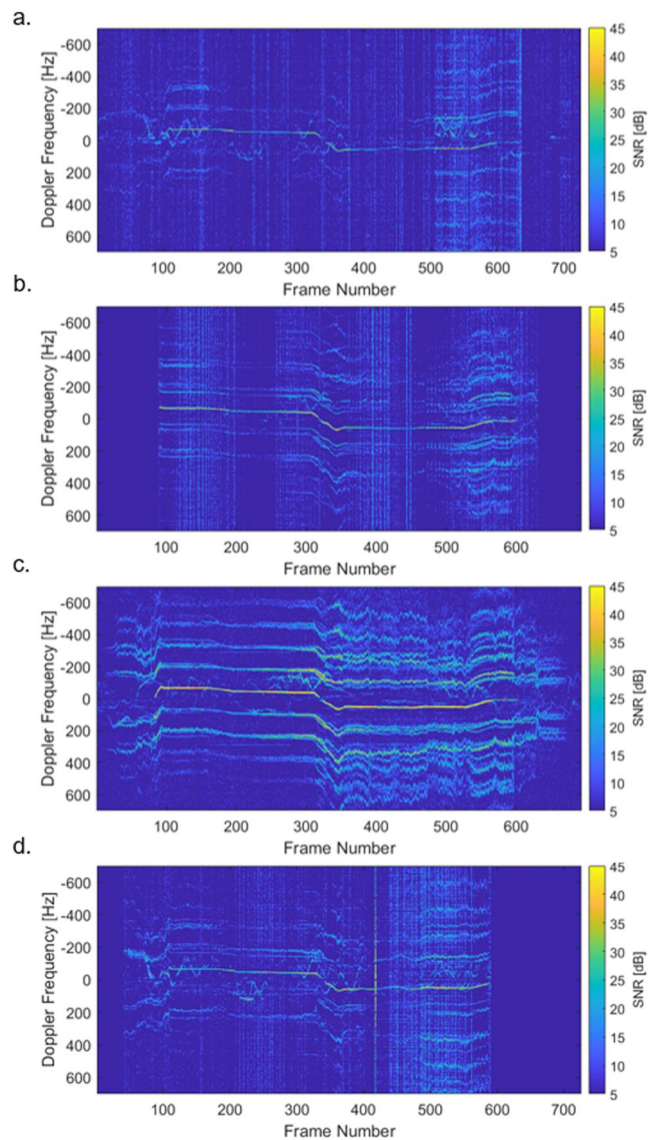


FIGURE 16 Target spectrograms for the DJI Inspire 3 drone target during the ADRAN trials. (a) Radar #1 monostatic, (b) Radar #1 bistatic, (c) Radar #2 monostatic, and (d) Radar #2 bistatic.

overall clutter power due to the radar geometry. The SNR recorded from the bistatic data sets are similar to each other but more closely resemble that of monostatic radar #1. There is a similar probability of detection (PD) in all data sets and is limited by the drone dead time while it is hovering in all flights but the in flight PD is higher for radar #1 when it is in bistatic mode rather than monostatic surprisingly. It is important to note one shortfall of the bistatic radar in these trials. Due to the significant timing error between the two radar nodes and the fact that this increases with time, there becomes a point where the timing error exceeds that of the recording window of the radar. At this point the direct signal is missing until it loops back around into the next PRI. This characteristic can be seen in Figure 16 before frame 80 and in Figure 16d after frame 600 where there is no data available. To solve this, the overall timing error of the radars cannot exceed the recording interval of the radar. Therefore the oscillators themselves

should be better synchronized in frequency either by steering to GNSS or by directly using frequency error information as feedback to steer one of the oscillators. However, this is beyond the scope of the current work.

The flight utilising radar #1 as monostatic and radar #2 as bistatic with DJI Inspire 3 as the controlled target was then analysed at the detection level. The raw data corresponding to the time of the flight was processed using the detector chain described in section 3.2. The detections were based on the SBM subtraction scheme with a set 20 dB threshold level and the results are compared with truth data. Detections for both the monostatic and bistatic radars were retrieved and the points relating to the controlled drone trial were extracted using a manual filtering method. The track was smoothed using a simple Savitzky-Golay filter to demonstrate the type of performance that would be achievable with this type of bistatic configuration. Figure 17a-b show the plan view of the tracks for the monostatic

TABLE 4 Quantitative measurements of SNR and detection probability for the different radar configurations.

Flight Number	Radar identifier and configuration	Median velocity [m/s]	Average SNR scaled [dB]	Max SNR scaled [dB]	Probability of detection
Flight 1	Radar #1 monostatic	8.1	38.78	57.71	0.664
Flight 1	Radar #2 passive	8.1	31.76	41.46	0.613
Flight 2	Radar #1 passive	8.7	37.33	53.91	0.726
Flight 2	Radar #2 monostatic	8.7	48.28	56.74	0.749

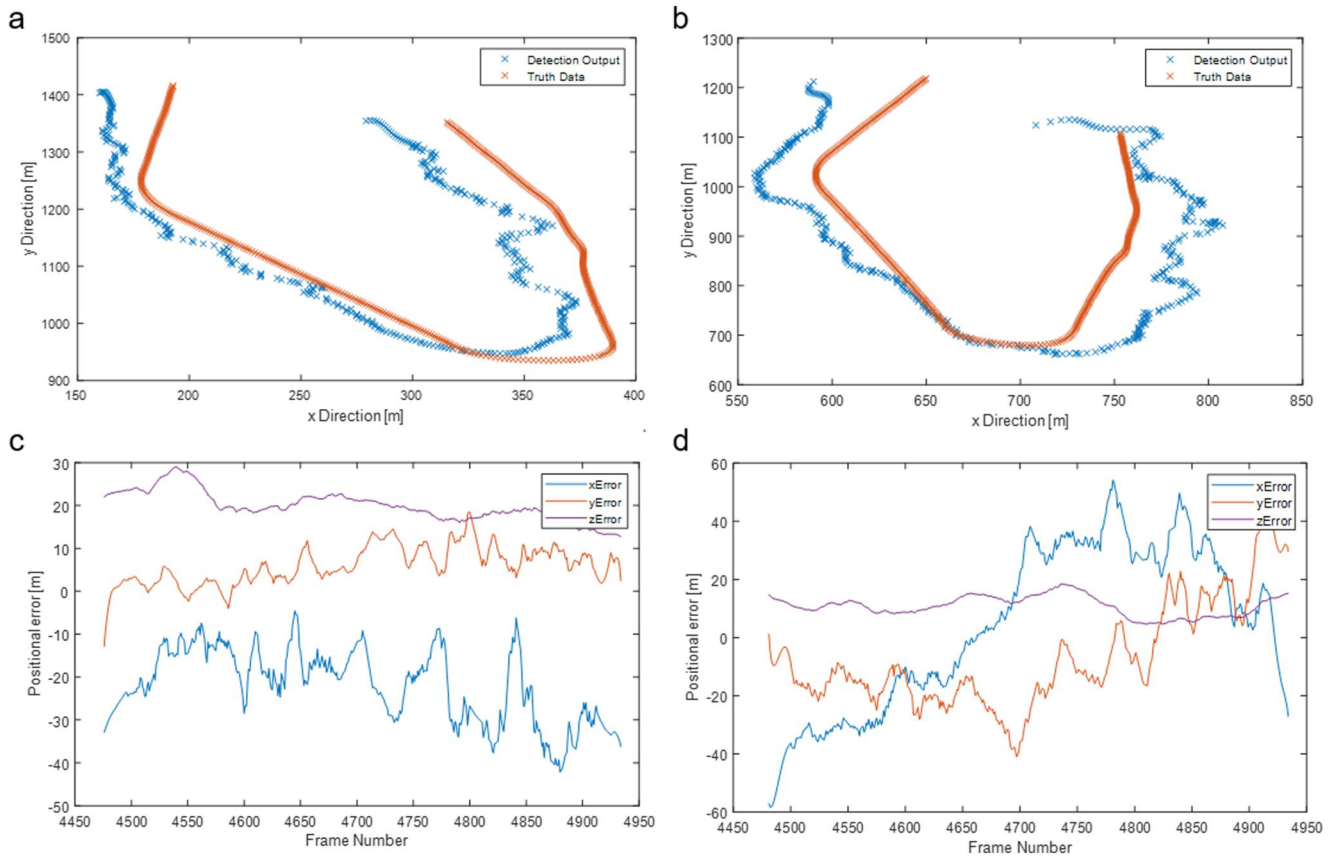


FIGURE 17 Positional accuracy measurements from a single controlled drone flight. (a) Plan view detection plot for monostatic radar #1, (b) Plan view detection plot for bistatic radar #2, (c) Positional error from truth radar #1, and (d) Positional error from truth radar #2.

and bistatic radars respectively with the truth data plotted for comparison. This demonstrates successful detection of the drone target throughout the flight with the bistatic radar node using the upgraded direct signal synchronisation scheme and the track matches well with the truth data in both cases. One of the main factors for the offset in both cases is a systematic bias in the elevation and azimuth angles due to multipath reflections. The positional error of the drone in local Cartesian coordinates is shown in Figure 17c-d. It is observed that while the error is generally less in the monostatic case, the height of the target was more accurately measured with the bistatic radar, possibly suggesting that the effect of multipath is reduced. However, the error in the x and y position fluctuate more in the bistatic radar due to the limited synchronisation accuracy corresponding to half of a range gate.

Overall, these results demonstrate the successful implementation of the improved direct signal synchronisation method in networked staring radar systems operating in an urban environment. Successful detection and localisation of S-UAV targets with performance levels comparable to the monostatic case. In general, the performance is slightly worse in the bistatic configurations but that is expected. The bistatic nodes are expected to provide considerable benefits when they are used in data fusing algorithms to enhance the detection accuracy as the networked configuration provides an opportunity for a potentially low cost upgrade of the standard monostatic system.

7 | CONCLUSION

This paper shows how it is possible to provide bistatic operation with a simplified approach that does not require pulse chasing. Here, a software-defined approach has been developed to create the synchronisation in a non-coherent pair of staring radars, retrieving the information from the direct breakthrough signal of the transmitter. The new updated approach also allows large stationary structures within the FOV to contribute to the measurement of range offset and allows this method to work when the direct signal is within the backlobe of the receiver beam or is obstructed. Time domain simulations of the radars were developed and have the capability to be scaled up to any number of nodes forming a network. The effect of synchronisation error was demonstrated in an urban simulated scenario and bistatic processing was verified on the synthetic data. Initial experimental field trials were performed with the ADRAN network using non-coherent oscillators. The direct signal synchronisation processing was successfully used to correct the time and frequency offset. Successful detection and tracking of drone targets in the bistatic configuration were achieved with SNR values and positional accuracy comparable to the monostatic configuration. Limitations of this configuration are the slower processing time required for generating SBM and for direct signal synchronisation, together with the lost data when a frequency drift is present and the direct signal drifts outside the recording window.

Future work will seek to improve the synchronisation using GPS disciplined oscillators or alternatively, another more stable and accurate clock such as caesium clocks or hydrogen

masers in each radar node to ensure the frequencies are locked. The long term drift and time error can then be monitored to determine if this is sufficient for the radars to function without any degradation in performance. In the long term, the radars will utilise photonic microwave oscillators to improve the short term stability of the radars to improve phase noise and overall sensitivity. Then, the optical source within the microwave photonic oscillator can be locked to optical lattice clocks for instance [54, 55], which can be used to improve the long term stability to the levels unprecedented in current radar systems and realise the quantum enabled radar network [18].

AUTHOR CONTRIBUTIONS

Darren Griffiths: Conceptualisation; Data curation; Formal analysis; Investigation; Methodology; Resources; Software; Validation; Visualisation; Writing – original draft; Writing – review & editing. **Mohammed jahangir:** Investigation; Resources; Software; Supervision; Writing – review & editing. **Jithin Kannanthara:** Investigation; Software; Validation; Visualisation; Writing – review & editing. **Gwynfor Donlan:** Software; Validation; Writing – review & editing. **Chris J. Baker:** Conceptualisation; Funding acquisition; Investigation; Project administration; Supervision; Validation; Writing – review & editing. **Michail Antoniou:** Funding acquisition; Methodology; Project administration; Resources; Writing – review & editing. **Yeshpal Singh:** Conceptualisation; Funding acquisition; Project administration; Resources; Supervision; Writing – review & editing.

ACKNOWLEDGEMENTS

This research is supported by a DSTL funded PhD and UK National Quantum Technology Hub in Sensing and Timing (EP/T001046/1) projects. The author thanks the Microwave integrated systems laboratory (MISL) team for contribution in data collection for the radar trials.

CONFLICT OF INTEREST STATEMENT

None

DATA AVAILABILITY STATEMENT

The data that support the findings of this study are available from Thales. Restrictions apply to the availability of these data, which were used under license for this study. Data are available from the authors with the permission of Thales.

ORCID

Darren Griffiths  <https://orcid.org/0000-0003-3194-439X>

Mohammed Jahangir  <https://orcid.org/0000-0002-5847-380X>

Jithin Kannanthara  <https://orcid.org/0000-0002-6156-1181>

REFERENCES

1. Sathyamoorthy, D.: A review of security threats of unmanned aerial vehicles and mitigation steps. *The Journal of Defence and Security* 6(1), 81–97 (2015)

2. Yaacoub, J.P., et al.: Security analysis of drones systems: attacks, limitations, and recommendations. *Internet of Things (Netherlands)* 11, 100218 (2020). Available from. <https://doi.org/10.1016/j.iot.2020.100218>
3. Merkert, R., Bushell, J.: Bushell, J.: Managing the drone revolution: a systematic literature review into the current use of airborne drones and future strategic directions for their effective control. *J. Air Transport. Manag.* 89(August), 101929 (2020). Available from. <https://doi.org/10.1016/j.jairtraman.2020.101929>
4. Jian, M., Lu, Z., Chen, V.C.: Drone detection and tracking based on phase-interferometric Doppler radar. In: 2018 IEEE Radar Conference, Radar Conf 2018, pp. 1146–1149 (2018)
5. Quevedo, D.A.D., et al.: Drone detection with x-band ubiquitous radar. *Proceedings International Radar Symposium*, 1–10 (2018)
6. Nuss, B., et al.: MIMO OFDM radar system for drone detection. *Proceedings International Radar Symposium*, 1–9 (2017)
7. Bounaceur, H., Khenchaf, A., Le.Caillec, J.M.: Analysis of small sea-surface targets detection performance according to airborne radar parameters in abnormal weather environments. *Sensors* 22(9), 3263 (2022). <https://doi.org/10.3390/s22093263>
8. Caris, M., et al.: Detection of small UAS with W-band radar. In: *Proceedings International Radar Symposium*, pp. 1–6 (2017)
9. Colin, J.M.: Phased array radars in France: present & future. In: *IEEE International Symposium on Phased Array Systems and Technology*, pp. 458–462 (1996)
10. Kinghorn, T., Scott, I., Totten, E.: Recent advances in airborne phased array radar systems. In: *IEEE International Symposium on Phased Array Systems and Technology*, pp. 1–7 (2016)
11. Jahangir, M., Baker, C.J.: Extended dwell Doppler characteristics of birds and micro-UAS at l-band. In: *Proceedings International Radar Symposium*, pp. 1–10 (2017)
12. Ritchie, M., et al.: Monostatic and bistatic radar measurements of birds and micro-drone. In: 2016 IEEE Radar Conference, Radar Conf, pp. 6–10 (2016)
13. Adrian, O.: From AESA radar to digital radar for surface-based applications. In: *IEEE National Radar Conference - Proceedings*, pp. 1–5 (2009)
14. Harman, S.: *Holographic Radar Development* (2021)
15. Aldowesh, A., Alnuaim, T., Alzogaiby, A.: Slow-moving micro-UAV detection with a small scale digital array radar. In: 2019 IEEE Radar Conference, Radar Conf 2019, pp. 1–5 (2019)
16. UrzaizQuevedo, D.F.I.Ã.D., et al.: Drone detection and radar-cross-section measurements by RAD-DAR. *IET Radar, Sonar Navig.* 13(9), 1437–1447 (2019). <https://doi.org/10.1049/iet-rsn.2018.5646>
17. Jahangir, M., et al.: Networked Staring Radar Testbed for Urban Surveillance: Status and Preliminary Results, pp. 471–476 (2023)
18. Jones, J.M., et al.: ‘Quantum enabled radar sensing’. In: 2022 IEEE International Topical Meeting on Microwave Photonics, MWP 2022 - Proceedings, pp. 1–4 (2022)
19. Wellig, P., et al.: Radar systems and challenges for C-UAV. *Proceedings International Radar Symposium 2018-June*, 1–8 (2018)
20. Baker, C.: *Netted Radar Sensing*, pp. 19–39. IEE Conference Publication (2005)
21. Ivashko, I., Leus, G., Yarovoy, A.: Radar network topology optimization for joint target position and velocity estimation. *Signal Process.* 130, 279–288 (2017). Available from: <https://doi.org/10.1016/j.sigpro.2016.07.010>
22. Dong, J., et al.: Advances in multi-sensor data fusion: algorithms and applications. *Sensors* 9(10), 7771–7784 (2009). <https://doi.org/10.3390/s91007771>
23. Griffiths, D., et al.: Direct Signal Synchronization for Staring Passive Bistatic Radar, pp. 220–225 (2023)
24. Nanzer, J.A., et al.: Distributed phased arrays: challenges and recent advances. *IEEE Trans. Microw. Theor. Tech.* 69(11), 4893–4907 (2021). <https://doi.org/10.1109/tmtt.2021.3092401>
25. Weiß, M.: Synchronisation of bistatic radar systems. In: *International Geoscience and Remote Sensing Symposium (IGARSS)* (2004)
26. Djenouri, D., Bagaa, M.: Synchronization protocols and implementation issues in wireless sensor networks: a review. *IEEE Syst. J.* 10(2), 617–627 (2016). <https://doi.org/10.1109/jysyst.2014.2360460>
27. He, Y., et al.: The impact of time synchronization error on passive coherent pulsed radar system. *Sci. China Inf. Sci.* 53(12), 2664–2674 (2010). <https://doi.org/10.1007/s11432-010-4110-x>
28. Hurley, S.M., et al.: Impact of synchronization on signal-to-noise ratio in a distributed radar system. In: *Proceedings 2006 IEEE/SMC International Conference on System of Systems Engineering* (2006)
29. Javadi, S.H., Farina, A.: Radar networks: a review of features and challenges. *Inf. Fusion* 61, 48–55 (2020). <https://doi.org/10.1016/j.inffus.2020.03.005>
30. Coluccia, A., Parisi, G., Fascista, A.: Detection and classification of multirotor drones in radar sensor networks: a review. *Sensors* 20(15), 1–22 (2020). <https://doi.org/10.3390/s20154172>
31. Ritchie, M., et al.: Multistatic micro-Doppler radar feature extraction for classification of unloaded/loaded micro-drones. *IET Radar, Sonar Navig.* 11(1), 116–124 (2017). <https://doi.org/10.1049/iet-rsn.2016.0063>
32. Alhuwaimel, S., et al.: First measurements with NeXtRAD, a polarimetric X/L Band radar network. In: 2017 IEEE Radar Conference, Radar Conf 2017, pp. 1663–1668 (2017)
33. Sandenbergh, J.S., Inggis, M.R.: A summary of the results achieved by the GPS disciplined references of the NetRAD and NeXtRAD multistatic radars. 2019 IEEE Radar Conference, Radar Conf(2), 1–6 (2019)
34. Guo, X., et al.: Micro-Doppler based mini-UAV detection with low-cost distributed radar in dense urban environment’. In: *EuRAD 2019 - 2019 16th European Radar Conference*, pp. 189–192 (2019)
35. Caris, M., et al.: Detection and tracking of micro aerial vehicles with millimeter wave radar. In: *Microwaves Everywhere”, EuMW 2016 - Conference Proceedings; 46th European Microwave Conference*, pp. 1553–1555. EuMC (2016)
36. Inggis, M.R., et al.: Report on the 2018 trials of the multistatic NeXtRAD dual band polarimetric radar’. In: 2019 IEEE Radar Conference, Radar Conf (2019)
37. Beasley, P.J., Ritchie, M.A.: Multistatic Radar Synchronisation Using COTS GPS Disciplined Oscillators, pp. 429–434 (2023)
38. Griffiths, H., Baker, C.: *An Introduction to Passive Radar* (2017)
39. Griffiths, H., Willis, N.: Klein Heidelberg - the first modern bistatic radar system. *IEEE Trans. Aero. Electron. Syst.* 46(4), 1571–1588 (2010). <https://doi.org/10.1109/taes.2010.5595580>
40. Brisken, S., et al.: Passive radar imaging using DVB-S2. In: 2017 IEEE Radar Conference, Radar Conf, pp. 0552 (2017)
41. Guo, H., Woodbridge, K., Baker, C.J.: Evaluation of WiFi beacon transmissions for wireless based passive radar. In: 2008 IEEE Radar Conference, RADAR, pp. 1–6 (2008)
42. Pastina, D., et al.: Passive radar imaging of ship targets with GNSS signals of opportunity. *IEEE Trans. Geosci. Rem. Sens.* 59(3), 2627–2642 (2021). <https://doi.org/10.1109/tgrs.2020.3005306>
43. Samczy, P., et al., pp. 60. *5G Network-Based Passive Radar* (2022)
44. Del Hoyo, G.P., Gronowski, K., Samczynski, P.: The STARLINK-based passive radar: preliminary study and first illuminator signal measurements. *Proceedings International Radar Symposium*, 350–355 (2022)
45. Razavi, B.: RF transmitter architectures and circuits. *Proceedings of the Custom Integrated Circuits Conference*, 197–204 (1999)
46. Floyd, B., et al.: A silicon 60GHz receiver and transmitter chipset for broadband communications. *Digest Tech. Pap. IEEE Int. Solid State Circ. Conf.* 41(12), 2820–2831 (2006). <https://doi.org/10.1109/jssc.2006.884820>
47. Rubio-CidreBadolatoCidre, G.A.G., et al.: DDS-based signal-generation architecture comparison for an imaging radar at 300 GHz. *IEEE Trans. Instrum. Meas.* 64(11), 3085–3098 (2015). <https://doi.org/10.1109/tim.2015.2440557>
48. Ng, H.J., Feger, R., Stelzer, A.: A fully-integrated 77-GHz UWB pseudo-random noise radar transceiver with a programmable sequence generator in SiGe technology. *IEEE Transactions on Circuits and Systems I: Regular Papers* 61(8), 2444–2455 (2014). <https://doi.org/10.1109/tcsi.2014.2309774>

49. Ghelfi, P., et al.: A fully photonics-based coherent radar system. *Nature* 507(7492), 341–345 (2014). Available from. <https://doi.org/10.1038/nature13078>
50. Richards, M.A., Scheer, J.A., Holm, W.A.: *Principles of Modern Radar: Basic Principles* (2010)
51. Willis, N.J.: 'Bistatic Radar'. (2004)
52. Marlow, B.L.S., Scherer, D.R.: A review of commercial and emerging atomic frequency standards. *IEEE Trans. Ultrason. Ferroelectrics Freq. Control* 68(6), 2007–2022 (2021). <https://doi.org/10.1109/tuffc.2021.3049713>
53. Goldman, S.J.: *Phase Noise Analysis in Radar Systems Using Personal Computers* (1989). <https://tudelft.on.worldcat.org/oclc/839683698>
54. Jha, A., et al.: 'Towards the development of an optical lattice clock testbed setup for the iqClock Project. In: 2023 Conference on Lasers and Electro-Optics Europe & European Quantum Electronics Conference, pp. 1. CLEO/Europe-EQEC) (2023)
55. Gellesch, M., et al.: An optical lattice clock testbed system for the iqClock Project demonstrator. In: IFCS-ISAF 2020 - Joint Conference of the IEEE International Frequency Control Symposium and IEEE International Symposium on Applications of Ferroelectrics, Proceedings, pp. 1–2 (2020)

How to cite this article: Griffiths, D., et al.: Fully digital, urban networked staring radar: simulation and experimentation. *IET Radar Sonar Navig.* 1–17 (2023). <https://doi.org/10.1049/rsn2.12499>